International Journal of Heat and Fluid Flow 102 (2023) 109148

Contents lists available at ScienceDirect

International Journal of Heat and Fluid Flow

journal homepage: www.elsevier.com/locate/ijhff

Scaling of secondary flows with surface parameters: A linear approach

Gerardo Zampino *, Davide Lasagna, Bharathram Ganapathisubramani

Faculty of Engineering and Physical Sciences, University of Southampton, Bolderwood Innovation Campus, Southampton, SO17 1BJ, Hampshire, UK

ARTICLE INFO

Keywords:
Linearized RANS equations
Secondary currents
Ridge-type roughness

ABSTRACT

Secondary flows are generated when a lateral variation of the topography, such as streamwise aligned ridges, is imposed upon a turbulent wall-bounded flow. In this case, the time-averaged flow field is characterized by streamwise vortices known as Prandtl's vortices of the second kind (Prandtl, 1952). As demonstrated in previous experimental and numerical works, the strength and flow organization of these vortices depend on the ridge shape. In this paper, the effect of the ridge geometry on the generation of secondary flows is investigated using the linearized RANS-based model proposed by Zampino et al. (2022). The model is derived from the assumption that the ridges are shallow, with height smaller than any other length scale, e.g. the viscous length scale. Symmetric channels with rectangular, triangular, elliptical and trapezoidal ridges are studied. The model predicts that the strength of secondary flows can be scaled with the mean ridge height, regardless of the ridge shape, when the ridges are narrower than the half channel height and isolated, i.e. when the lateral separation between the ridges is much larger than the ridge width. Finally, the appearance of tertiary flows and the effect of the ridge shape on the flow organization is studied in detail for trapezoidal geometries. It is observed that tertiary flows emerge for ridge configurations where the scaling behaviour does not hold.

1. Introduction

The generation of secondary flows, or currents , over a surface with heterogeneous attributes, such as a lateral variation of the roughness height or of the wall topography, is largely studied in literature. Secondary currents are known as Prandtl's vortices of the second kind (Prandtl, 1952) and they consist of counter-rotating, time-averaged, streamwise-aligned vortices embedded in the primary wall-bounded flow, e.g. channel flow or boundary layer flow. Since the first experiments conducted by Hinze (1967), these structures have gained increasing importance in industrial applications because secondary flows alter and modify the performances of fluid dynamics surfaces such as the transport properties of wall-bounded flows (Volino et al., 2011; Mejia-Alvarez and Christensen, 2013; Vanderwel and Ganapathisubramani, 2015; Hwang and Lee, 2018; Medjnoun et al., 2020; Zampiron et al., 2020), the heat transfer (Stroh et al., 2020) and the aerodynamic performances (Jiménez, 2004; Mejia-Alvarez and Christensen, 2013). For surfaces with topographical heterogeneity, with alternating regions of high/low relative elevation (Hwang and Lee, 2018; Medjnoun et al., 2018, 2020; Castro et al., 2021), the flow organization is characterized by alternating high-momentum pathways (HMPs) and low-momentum pathways (LMPs) corresponding to a downwash/upwash motion respectively (Barros and Christensen, 2014; Willingham et al., 2014). These structures were observed both experimentally (Anderson et al., 2015) and numerically (Stroh et al., 2016; Chung et al., 2018). It has been shown that the HMPs and LMPS differ in terms of the production and dissipation rate as a function of the ridges shape (Medjnoun et al., 2020) but how the geometry affects the generation mechanism of secondary structures and their strength is not fully clear. Some authors (Wu and Christensen, 2007; Castro et al., 2021) observed that, in some cases, secondary flows over different geometries appear to be similar and this suggests a possible scaling of the secondary flows with a geometrical property of the surface. In particular, Castro et al. (2021) concluded that the strength of the secondary flows developing over rectangular ridges depends on the ratio between the ridge spacing and width and the flow organization is independent of the spacing between the ridges when scaled with the channel height. Other scaling geometrical parameters have been proposed in the literature, such as the ratio between the wetted area above and below the ridge mean height by Medjnoun et al. (2020).

In this paper, we consider these aspects by using the model proposed in our previous work (Zampino et al., 2022). The model is based on the linearized Reynolds-Averaged Navier–Stokes (RANS) equations, augmented with the Spalart–Allmaras (SA) turbulence model (Spalart and Allmaras, 1994) for the closure. The model approximates the response of the turbulent wall-bounded flow in the specific regime where the topography variations of the surface are small, smaller than the smallest relevant length scale, i.e. the viscous length. From a practical

* Corresponding author.
E-mail address: g.zampino@soton.ac.uk (G. Zampino).

https://doi.org/10.1016/j.ijheatfluidflow.2023.109148
Received 6 December 2022; Received in revised form 21 April 2023; Accepted 2 May 2023
Available online 24 May 2023
0142-727X/© 2023 The Author(s). Published by Elsevier Inc. This is an open access article under the CC BY license (http://creativecommons.org/licenses/by/4.0/).

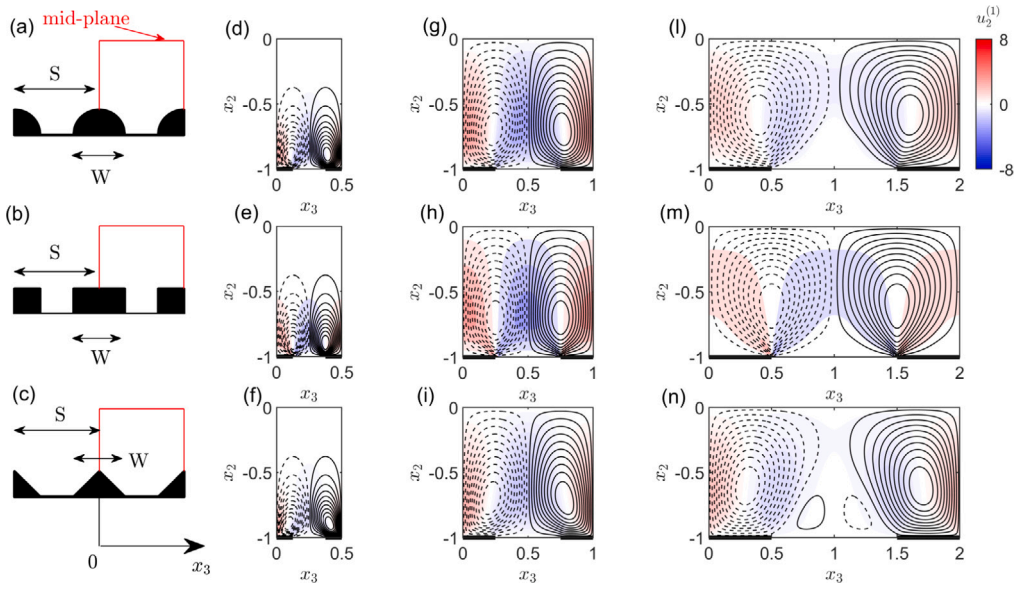

Fig. 1. Contour lines of the perturbation streamfunction $\psi^{(1)}$ at $Re_\tau = 1000$ and for elliptical ridges (top panels), rectangular ridges (central panels) and triangular ridges (bottom panels). Dashed lines are used for negative values. A sketch of the cases studied is reported in panels (a,b,c). The flow organization is shown for the bottom half channels in the region delimited by the red lines. The colour map of the wall-normal velocity perturbation $u_2^{(1)}$ is also reported to better display the flow organization above the ridges. The duty cycle $DC = 0.5$ for all cases while the width varies from 0.25 (left column) 0.5 (central column) and 1 (right column). To help the reader, a simplified representation of the ridges is reported at the bottom of each plot (bold black lines).

standpoint, this regime corresponds to "hydraulically smooth ridges" well submerged in the viscous sub-layer. With this assumption, the lateral variation of the topography can be modelled using linearized boundary conditions (Russo and Luchini, 2016). This results in a rather simple mathematical model that can be inspected and evaluated very rapidly to explore a wide range of topographies, and obtain new insight on the interaction between the topography and the turbulent flow.

In Zampino et al. (2022), the tool was utilized to study the generation of secondary flows in symmetric channels with harmonic wall modulations and rectangular ridges. The main contribution of this paper is to extend the analysis to other commonly studies ridge geometries, i.e. elliptical, triangular and trapezoidal ridges. The goal is to examine the role of the ridge geometry in determining the strength and the topology of secondary currents and identify regions where such quantities can be scaled with appropriate surface parameters.

A brief description of the modelling procedure proposed in our previous work is first reported in Section 2. Then, the model is applied to rectangular, elliptical and triangular ridges in Section 3, followed by a discussion on the scaling of the strength of secondary flows with geometric parameters in Sections 4 and 5. The analysis of the flow organization over trapezoidal ridges and the discussion about the generation mechanism of the tertiary flows are reported in Section 6. Finally, conclusions and limitations of the approach are summarized in Section 7.

2. Linearized RANS model

A pressure-driven channel with streamwise aligned ridges symmetrically placed on the lower and upper walls is studied. The streamwise, wall-normal and spanwise directions, normalized with the channel half height h, are identified by the Cartesian coordinates (x_1, x_2, x_3) respectively. The coordinate system is centred on the channel mid-plane. The flow is governed by the continuity and the momentum equations for the velocity components (u_1, u_2, u_3) scaled with the friction velocity $u_\tau = \sqrt{\tau_w/\rho}$, with $\tau_w = h\Pi$ the mean wall friction and where Π is the constant pressure gradient. Given these definitions, $Re_\tau = u_\tau h/\nu$ is the friction Reynolds number. The Reynolds decomposition produces the mean velocity $\overline{u}_i$ and the fluctuation u_i'. The nondimensional Reynolds-averaged continuity and momentum equations are

$$\frac{\partial \overline{u}_i}{\partial x_i} = 0, \tag{1}$$

$$\overline{u}_j \frac{\partial \overline{u}_i}{\partial x_j} = -\delta_{i1} + \frac{1}{Re_\tau}\frac{\partial^2 \overline{u}_i}{\partial x_j^2} - \frac{\partial \overline{u_i' u_j'}}{\partial x_j}, \tag{2}$$

where the overbar indicates a time-averaged quantity. Note that, in these equations and in what follows, the velocity is always scaled with u_τ, but the superscript $(^+)$ is not used to avoid cluttering the notation. We assume that the mean flow is streamwise independent, i.e. $\partial(\bar{\cdot})/\partial x_1 \equiv 0$, when considering flows that develop over streamwise aligned ridges. Hence, the mean pressure can be eliminated by employing a streamwise velocity/streamfunction formulation, where the streamfunction $\overline{\psi}$ satisfies $\nabla^2 \overline{\psi} = \overline{\omega}_1$ with

$$\overline{\omega}_1 = \frac{\partial \overline{u}_3}{\partial x_2} - \frac{\partial \overline{u}_2}{\partial x_3} \tag{3}$$

being the time-averaged streamwise vorticity.

A sketch of the ridge geometries considered in this paper is reported in Fig. 1(a,b,c), where S is the spacing between the ridges and W is the ridge width. The duty cycle DC is defined as W/S. These geometries are described in the model by the zero-mean function $f(x_3)$, with unit peak-to-peak amplitude. The lower and upper channel surfaces are thus symmetrically placed at $x_2 = \mp 1 \pm \epsilon f(x_3)$, where ϵ controls the peak-to-peak ridge height.

The proposed methodology is based on decomposing the flow field into a homogeneous flow developing in the flat channel and a flow perturbation induced by the ridges. Hence, we expand any time-averaged flow quantity q using a Taylor series in the amplitude ϵ as

$$q(x_2, x_3) = q^{(0)}(x_2) + \epsilon q^{(1)}(x_2, x_3) + \mathcal{O}(\epsilon^2), \tag{4}$$

where the zero-order term $q^{(0)}$ is the base flow solution in the flat channel and the first-order term $q^{(1)}$ is the flow response per unit of ridge height. Note that the overbar is dropped in the following sections to avoid cluttering the notation. Following Russo and Luchini (2016), we assume that the ridge height is smaller that any other length scale ($\epsilon \ll 1$), i.e. much smaller than the viscous length scale. From a practical standpoint, this regime corresponds to "hydraulically

smooth ridges" that are well submerged in the viscous sub-layer. Thus, in Eq. (4) higher order terms in ϵ are neglected. Substituting the Taylor expansion (4) in the governing equations written using the streamwise velocity/ streamfunction formulation and considering terms at order one in ϵ, we obtain the set of linear RANS equations:

$$-\frac{\partial \psi^{(1)}}{\partial x_3}\Gamma = \frac{1}{Re_\tau}\left(\frac{\partial^2}{\partial x_2^2}+\frac{\partial^2}{\partial x_3^2}\right)u_1^{(1)} + \frac{\partial \tau_{12}^{(1)}}{\partial x_2}+\frac{\partial \tau_{13}^{(1)}}{\partial x_3}, \tag{5}$$

$$0 = \frac{1}{Re_\tau}\left(\frac{\partial^2}{\partial x_2^2}+\frac{\partial^2}{\partial x_3^2}\right)^2 \psi^{(1)} + \frac{\partial^2}{\partial x_2 \partial x_3}\left(\tau_{33}^{(1)}-\tau_{22}^{(1)}\right)+\left(\frac{\partial^2}{\partial x_2^2}-\frac{\partial^2}{\partial x_3^2}\right)\tau_{23}^{(1)}, \tag{6}$$

where Γ is the zero-order streamwise velocity wall-normal gradient and $\tau_{ij}^{(1)}$ is the Reynolds stress tensor perturbation.

The tensor $\tau_{ij}^{(1)}$ must be expressed as a function of other mean quantities. As already discussed in the literature of noncircular ducts (Perkins, 1970; Bottaro et al., 2006), when the linear Boussinesq's hypothesis is used, no secondary flows can be predicted because the streamwise momentum Eq. (5) and the streamfunction Eq. (6) are decoupled. Hence, a nonlinear Reynolds stress model is necessary for the correct prediction of anisotropic stresses that are the source of the secondary flows. Many approaches have been described in the literature (Speziale et al., 1991; Speziale, 1991; Chen et al., 1997). In this work, we used the Quadratic Constitutive Relation (QCR) nonlinear model introduced in Spalart (2000). The QCR model contains simple terms proportional to the product of the rotation and the strain tensors. This model was recently utilized by Spalart et al. (2018) to predict the high-Reynolds number asymptotic properties of secondary flows in square and elliptical ducts, providing a good approximation of the secondary vortical flow topology and of the wall friction coefficient. In the QCR, the Reynolds stresses become

$$\tau_{ij} = \tau_{ij}^L - C_{r1}\left[O_{ik}\tau_{jk}^L + O_{jk}\tau_{ik}^L\right], \tag{7}$$

where O_{ik} is the normalized rotation tensor

$$O_{ij} = \frac{2W_{ij}}{\sqrt{\frac{\partial \overline{u}_m}{\partial x_n}\frac{\partial \overline{u}_m}{\partial x_n}}}, \quad \text{with} \quad W_{ij} = \frac{1}{2}\left(\frac{\partial \overline{u}_i}{\partial x_j}-\frac{\partial \overline{u}_j}{\partial x_i}\right) \tag{8}$$

and $\tau_{ij}^L = \nu_t S_{ij}$ is the linear Reynolds stress tensor from the Boussinesq's approximation with S_{ij} the mean velocity gradient tensor and ν_t the eddy viscosity. The constant $C_{r1} = 0.3$ is calibrated to match the anisotropy in the outer region over wall-bounded turbulent flows following Spalart (2000).

Previous studies that have utilized linearized RANS equations to describe the transient growth of secondary flows in turbulent channels (del Álamo and Jiménez, 2006; Pujals et al., 2009) have used analytical eddy-viscosity profiles (Cess, 1958; Reynolds and Hussain, 1972). In the present paper, in order to provide the eddy viscosity distribution above the modulated geometry and capture transport effects, we use the Spalart–Allmaras (SA) eddy viscosity transport model (Spalart and Allmaras, 1994). In the SA model the eddy viscosity ν_t is related to the modified eddy viscosity $\tilde{\nu}$ by the formula

$$\nu_t = \tilde{\nu} f_{v1} \tag{9}$$

where

$$f_{v1} = \frac{\chi^3}{\chi^3 + c_{v1}^3} \tag{10}$$

and $\chi = Re_\tau \tilde{\nu}$. The linearized transport equation for the perturbation of the modified eddy viscosity $\tilde{\nu}^{(1)}$ is

$$-\frac{\partial \psi^{(1)}}{\partial x_3}\frac{\partial \tilde{\nu}^{(0)}}{\partial x_2} = \frac{1}{\sigma}\left(\frac{1}{Re_\tau}+\tilde{\nu}^{(0)}\right)\left(\frac{\partial^2}{\partial x_2^2}+\frac{\partial^2}{\partial x_3^2}\right)\tilde{\nu}^{(1)} + \frac{1}{\sigma}\frac{\partial^2 \tilde{\nu}^{(0)}}{\partial x_2^2}\tilde{\nu}^{(1)}$$
$$+ \frac{1}{\sigma}(2+2c_{b2})\frac{\partial \tilde{\nu}^{(0)}}{\partial x_2}\frac{\partial \tilde{\nu}^{(1)}}{\partial x_2} + c_{b1}\tilde{\nu}^{(0)}\tilde{\mathcal{S}}^{(1)} + c_{b1}\tilde{\nu}^{(1)}\tilde{\mathcal{S}}^{(0)}$$
$$-2\,\tilde{\nu}^{(0)}c_{w1}f_w^{(0)}\frac{\tilde{\nu}^{(1)}d^{(0)}-\tilde{\nu}^{(0)}d^{(1)}}{d^{(0)\,3}} - c_{w1}f_w^{(1)}\left(\frac{\tilde{\nu}^{(0)}}{d^{(0)}}\right)^2. \tag{11}$$

where $\tilde{\mathcal{S}}$ is defined as

$$\tilde{\mathcal{S}} = \sqrt{2W_{ij}W_{ij}} + \frac{\tilde{\nu}}{k^2 d^2}f_{v2} \quad \text{with} \quad f_{v2} = 1 - \frac{\chi}{1+\chi f_{v1}}. \tag{12}$$

A detailed description of the other terms in Eq. (11) is reported in Zampino et al. (2022).

The effect of the ridges is introduced with linearized boundary conditions (Luchini, 2013; Busse and Sandham, 2012). Expanding the velocity near the surface in a Taylor series in x_2 and enforcing the no-slip condition at the physical surface, the streamwise velocity component at the lower domain boundary is given by the inhomogeneous boundary condition

$$u_1^{(1)}\Big|_{x_2=-1} + f(x_3)\left.\frac{\partial u_1^{(0)}}{\partial x_2}\right|_{x_2=-1} = 0, \tag{13}$$

i.e. the perturbation velocity at the boundary of the numerical domain is proportional to the wall-normal gradient of the streamwise velocity in the plane channel. When substituting the definition (4) in Eq. (13) and considering only the terms at order one, the streamwise velocity perturbation becomes

$$u_1^{(1)}(x_2=-1) = -f(x_3)\left.\frac{\partial u^{(0)}}{\partial x_2}\right|_{x_2=-1} = -f(x_3)Re_\tau, \tag{14}$$

while $u_3^{(1)}(x_2=-1)=0$ and $u_2^{(1)}(x_2=-1)=0$. Similarly, inhomogeneous boundary conditions are derived for the perturbation eddy viscosity $\nu_t^{(1)}$ which vanishes at the physical surface.

The geometry of the wall is modelled by the cosine expansion

$$f(x_3) = \sum_{n=1}^{\infty} f^n \cos(nk_3 x_3), \tag{15}$$

where f^n is the amplitude of the nth wavenumber mode and $k_3 = 2\pi/S$ is the fundamental wavenumber. The amplitude coefficients are obtained by calculating analytically the Fourier transform of the geometries considered in this work. The coefficient f_0 is always set to zero for all geometries considered, i.e. only zero-mean modulations of the channel walls are considered. In fact, a change in the mean height only corresponds to a change of the Reynolds number, and has no impact on the formation of secondary structures.

With a periodic wall, a periodic solution to the linear Eqs. (5), (6) and (11) is sought for. Hence, the streamwise velocity, the streamfunction and the eddy viscosity are expanded in series as

$$\left\{u_1^{(1)}(x_2,x_3), \tilde{\nu}^{(1)}(x_2,x_3)\right\} = \sum_{n=1}^{\infty}\left\{\hat{u}_1(x_2;n), \hat{\nu}(x_2;n)\right\}\cos(nk_3x_3), \tag{16}$$

$$\psi^{(1)}(x_2,x_3) = \sum_{n=1}^{\infty}\hat{\psi}(x_2;n)\sin(nk_3x_3). \tag{17}$$

Substitution of these expansions into the governing equations results in one set of three coupled linear partial differential equations (PDEs) in the wall-normal direction for the quantities $\{\hat{u},\hat{v},\hat{\psi}\}$ at each wavenumber $n = 1,2,\ldots$ separately. These PDEs are then solved using standard Chebyshev discretization techniques. The flow response for any complex geometry can be obtained by appropriately combining the responses obtained at individual spanwise length scales, i.e. following the superposition principle.

The solution at order zero, consisting of wall-normal profiles of the streamwise velocity and the eddy viscosity in a flat channel, has been obtained from an in-house code based on the Chebyshev discretization method. The resulting coupled system of nonlinear algebraic equations, the streamwise momentum equation and the SA eddy viscosity

transport equation, has been solved with a Jacobian-free Newton–Krylov technique (Knoll and Keyes, 2004). Other numerical aspects are described in Zampino et al. (2022).

It is worth noting that the present linear model cannot predict changes of the skin friction drag resulting from the modulation of the wall geometry. To see why this is the case, consider a channel with infinite span where the wall geometry is given by the wave $f(x_3) = \cos(k_3 x_3)$ and the lower channel wall is at $x_2 = -1 + \epsilon f(x_3)$, where ϵ controls the amplitude of the modulation. One would expect that the overall drag produced in such a channel does not depend on the *sign* of ϵ, since changing the sign of ϵ is equivalent to a lateral displacement of the original geometry by half wavelength. Therefore, the friction coefficient in such a channel must be an even function of the amplitude ϵ and must obey the Taylor expansion $C_f(\epsilon) = C_f^{(0)} + 1/2\epsilon^2 C_f^{(2)} + \mathcal{O}(\epsilon^4)$, i.e. the first order term must be identically zero and terms at order two and above in ϵ need to be calculated. These would depend on high-order velocity perturbations that the present linear model does not provide. An equivalent explanation is that the first-order perturbation of the wall shear stress resulting from the expansion (16) of the perturbation streamwise velocity and computed from the present linear model has zero average over the span of the channel, for any geometry. In fact, with linear equations, a geometry modulation at a wave number $n \neq 0$ only produces velocity perturbations at the same wavenumber and has no effect on the average friction drag. The full nonlinear equations need to be solved to capture the $n = 0$ wavenumber change in the streamwise velocity generated from a $n \neq 0$ geometry modulation.

3. Linearized predictions of the flow organization

Firstly, secondary flows are predicted over elliptical, rectangular and triangular ridges at $Re_\tau = 1000$ with duty cycle $DC = W/S = 0.5$ and $W = 0.25$ (left panels), 0.5 (central panels) and 1.0 (right panels) in Fig. 1. Contours of the perturbation streamfunction $\psi^{(1)}$ and the colour map of the wall-normal velocity perturbation $u_2^{(1)}$ are also reported to better display the flow organization. Because symmetric channel configurations are studied, subjected to a periodic wall modulation, only the bottom half-channel and a single ridge period is here shown.

In previous work (Zampino et al., 2022), we observed that the Reynolds number affects only mildly the strength of secondary flows, with no effect on the flow organization. More specifically, for high Reynolds numbers, the solution of the present model becomes Reynolds invariant because of the turbulence model used. In fact, the Spalart–Allmaras model (Spalart and Allmaras, 1994) is built in order to obtain a collapse of the eddy viscosity profile in the logarithmic layer for high Reynolds numbers. As a consequence, the eddy viscosity profile and the Reynolds stresses are asymptotically Reynolds number independent when scaled with the friction velocity. For this reason, the results for $Re_\tau = 1000$ are reported here as representative of secondary flows generated at high Reynolds numbers.

For small spacing (left column), secondary flows predicted for all three geometries show an upwelling (downwelling) motion above the ridges (inside the troughs). The secondary currents occupy only about a quarter of the channel height and they are similar in size and strength for all three geometries considered. Although some differences are predicted in the very near-wall region where the ridge geometry affects the local time-averaged flow structures, these differences are weak and negligible. For increasing ridge width W, the vortices grow in size and strength until they occupy the entire channel half-height (central column). Some differences are here evident in the strength of secondary flows and stronger downwash velocity is predicted at the gap centre for rectangular ridges. For $W = 1$, very large streamwise vortices are observed for all geometries (right column). In particular, for rectangular ridges, the secondary flows are locked at the ridge edge due to the strong discontinuity introduced by the ridge geometry. The same feature is also observed for elliptical ridges where the secondary flows develop in proximity of the ridge edge. By contrast, for triangular ridges, the secondary currents occur at the flank of the ridge. For this case, weaker and smaller time-averaged vortical structures having an opposite rotational direction compared to the secondary flows, are predicted. For specific spacing and widths, these tertiary flows can also be observed at the centre of the trough for the other geometries when the gap between the ridges is large enough to allow streamwise vortices to fully develop. In fact, for large spacing, the secondary flows reach their maximum size and a further increase of the spacing allows tertiary flows to emerge. For similar reasons, tertiary flows can be predicted over the rectangular and elliptical ridges when the ridge width is large enough. By contrast, no tertiary flows over the ridge are observed for the triangular shape because the deflection of the spanwise velocity component induced by the flank of the ridges is weaker.

4. Scaling of the strength of secondary flows

The strength of secondary flows is not uniquely defined and different authors use different quantities to characterize it. As in our previous work (Zampino et al., 2022), we use the kinetic energy density $\mathcal{K}$, defined as the volume-averaged kinetic energy per unit mass of the cross-sectional perturbation velocity components:

$$\mathcal{K} = \frac{1}{4S}\int_0^S \int_{-1}^1 \left[u_2^{(1)}(x_2,x_3)^2 + u_3^{(1)}(x_2,x_3)^2\right] \mathrm{d}x_2\,\mathrm{d}x_3.$$

We also use the peak value over the domain of the streamfunction, i.e. the quantity $\max_{x_2,x_3} \psi^{(1)}(x_2,x_3)$, as an indication of the strength of the vortical structures. Many experimental and numerical works use the dispersive stresses

$$\sigma_{ij}(x_2) = \frac{1}{S}\int_0^S u_i^{(1)}(x_2,x_3)u_j^{(1)}(x_2,x_3)\mathrm{d}x_3$$

to study the generation of secondary flows. In order to characterize their global strength using a single scalar quantity, we also introduce the integral quantity

$$R_{ij}^l = \int_{-l}^{l} \sigma_{ij}(x_2)\mathrm{d}x_2, \tag{18}$$

where we take $l = 0.9$ to discard the contribution in the near-wall region in the immediate vicinity of the ridges, to only focus on the dispersive stresses produced by large-scale motions filling the full half-height of the channel.

Maps of the kinetic energy density $\mathcal{K}$ (top panels), of the maximum of the streamfunction $\max_{x_2,x_3} \psi^{(1)}$ (central panels) and the quantity $R_{12}^{0.9}$ (bottom panels) are plotted in Fig. 2 for $Re_\tau = 1000$, as a function of S and W for the three geometries considered. The maps have been obtained using 50 samples for both S and W. In a first approximation, the three quantities we introduced for the analysis of the strength of the secondary flows are equivalent and the predictions of the amplification of the secondary currents are unaffected by the quantity chosen. Thus, the maps of Fig. 2 only depend on the ridge geometry and, quite weakly, on the Reynolds number, as discussed previously.

Hereinafter, more general considerations are reported for all cases studied. The linear model predicts i) a region of high amplification at $(S,W) \approx (1.25, 0.67)$ where the strength of the secondary flows is maximum for all quantities considered (small difference in the position of the amplification geometry are observed as a function of the ridge shape), and (ii) high amplification along a line at constant $W \approx 0.67$ for increasing spacing. However, the peak values across the three cases are different (stronger for rectangular ridges), confirming that the strength of secondary currents depends on the ridge geometry. For large spacing S or width W, all quantities considered for rectangular ridges also displays a second amplification peak not visible for the other geometries and corresponding to the maximum strength of the tertiary flows developing at the ridge centre (or trough centre). This suggests that tertiary flows are generated in different configurations in terms of S and W, depending on the ridge shape. A complete analysis of the generation of tertiary flows as a function of the ridge shape and

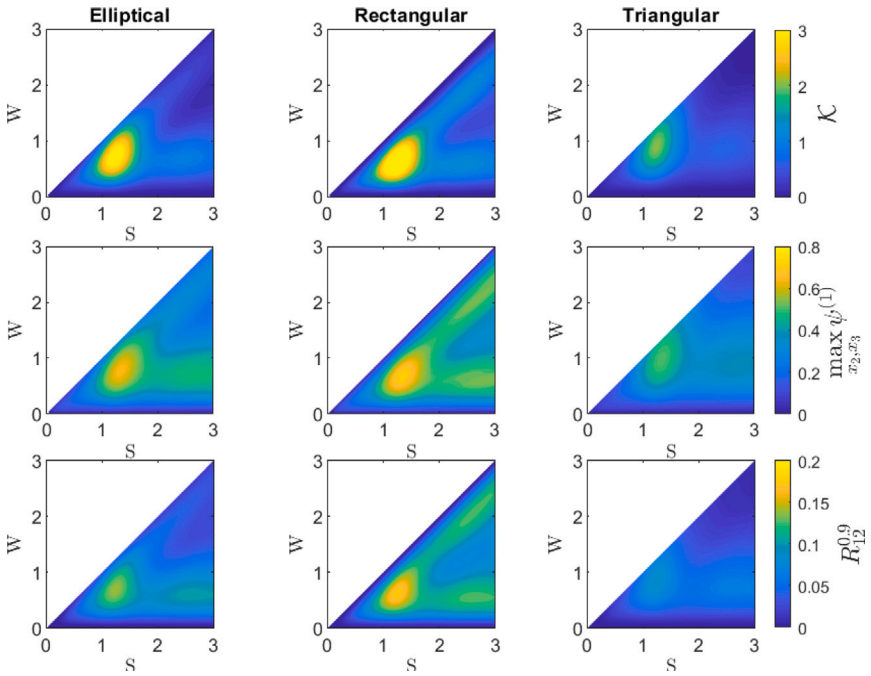

Fig. 2. Maps of the kinetic energy density $\mathcal{K}$ (top panels), the maximum of the streamfunction $\max_{x_2,x_3} \psi^{(1)}$ (central panels) and dispersive stress $\hat{R}_{12}^{0.9}$ (bottom panels) are reported as a function of the ridge spacing S and ridge width W for $Re_\tau = 1000$ for elliptical ridges (left column), rectangular ridges (central column) and triangular ridges (right column). The maps have been obtained using 50 samples for both S and W.

the effect of the ridge shape is reported in Section 6 where the flow organization is plotted for more complex shapes.

Despite the difference in the strength of the response, the flow organization observed for the narrow ridge case $W = 0.25$ shown in Fig. 1 is similar for all geometries, although the intensity of the cross-stream motion depends on the geometry. This fact suggest that the cross-stream velocities and, therefore, all derived quantities, might be scaled using an appropriate geometrical parameter. In this particular regime, when ridges are narrow and isolated one from the other, it can be argued that the surface perturbation generating the secondary currents is localized in a narrow region, and the strength of the surface perturbation is proportional to the ridge cross-sectional area, but not its geometry. For this reason, we introduce the mean ridge height, defined as

$$\overline{H} = \frac{A_r}{S},$$

i.e., the ratio between the ridge cross-sectional area A_r and the spacing S and use this quantity to scale the perturbation velocity field.

The maps of the scaled kinetic energy $\hat{\mathcal{K}}$ (top panels), the scaled maximum of the streamfunction $\max_{x_2,x_3} \hat{\psi}^{(1)}$ (central panels) and the scaled integral of the dispersive stress $\hat{R}_{12}^{0.9}$ (bottom panels) are reported in Fig. 3. The velocity profiles and the streamfunction are scaled with $\overline{H}$ while the kinetic energy, as well as the quantity $R_{12}^{0.9}$, is divided by the square of the mean ridge height $\overline{H}$ since it is given by the integral of a velocity squared. Explicitly, $\hat{\mathcal{K}}$ is given by $\mathcal{K}/\overline{H}^2$, $\hat{R}_{12}^{0.9}$ is equal to $R_{12}^{0.9}/\overline{H}^2$ and the maximum of the streamfunction scaled $\max_{x_2,x_3} \hat{\psi}^{(1)}$ is equal to $\max_{x_2,x_3} \psi^{(1)}/\overline{H}$. Note that, when scaling the strength of the secondary flows with the mean ridge height $\overline{H}$, the effective height of the ridges is constant and it is unitary for all cases studied. These maps show strong similarities for the region characterized by low ratio W/S *and* small W. We define these two areas of the parameter space, as summarized in Fig. 4, as the "isolated ridge" regime, where $W \ll S$ and ridges are small in width compared to the distance between one another (blue area), and the "narrow ridge" regime, where $W \ll 1$ and the ridges are narrow compared to the channel half-height (yellow area). The combination of these two regimes is displayed as a red area and it is defined in the following as the scaling region.

To better visualize this behaviour, we introduce the quantity

$$\Delta\hat{R}_{12}^{0.9}\% = \frac{\max \hat{R}_{12}^{0.9} - \min \hat{R}_{12}^{0.9}}{\text{mean } \hat{R}_{12}^{0.9}} \cdot 100, \tag{19}$$

where the function "max" is the maximum value obtained across the three geometries for a fixed configuration (S, W). Similarly, we define the functions "min" and "mean" as the minimum and the mean value, respectively. The quantity $\Delta\hat{R}_{12}^{0.9}\%$ can be interpreted as the difference in secondary flows strength across the three geometries for the same width and spacing. This quantity is plotted in Fig. 5. We can observe that the relative difference in scaled strength is small if the ridges are narrow and isolated. If this condition is not met, for configurations where the ridges are wide or tightly packed, the difference in the scaled dispersive stresses across the three geometries increases. These differences in the strength of secondary flows observed for elliptical, rectangular and triangular ridges can be easily explained as a consequence of the differences in the flow structures predicted for wide ridges. As observed for the flow topology in Fig. 1, tertiary flows emerge for the given S and W only for triangular ridges when the available space between the secondary flows is large enough.

5. Scaling of the velocity profiles

For a better characterization of the scaling of the secondary flows, the profiles of the velocity component divided by $\overline{H}$, for elliptical, triangular and rectangular ridges are reported in Fig. 6. Three cases are here considered for a constant spacing $S = 1.25$ and varying width in order to display the scaling behaviour for narrow *and* isolated ridges for $W = 0.2$ (left column), and the scaling breakdown for $W = 0.67$ (central column), corresponding to the maximum amplification configuration, and for $W = 1.0$ (right column), corresponding to wide ridges.

The wall-normal velocity profiles for the three geometries at the ridge centre and at the centre of the trough are reported in the top and central panels, respectively. The spanwise velocity component at the ridge edge is also provided in the bottom panels. The wall-normal velocity $u_2^{(1)}/\overline{H}$ at the ridge centre (top panels) collapses in the far-wall region only for $W = 0.2$ whereas for increasing ridge width the scaled

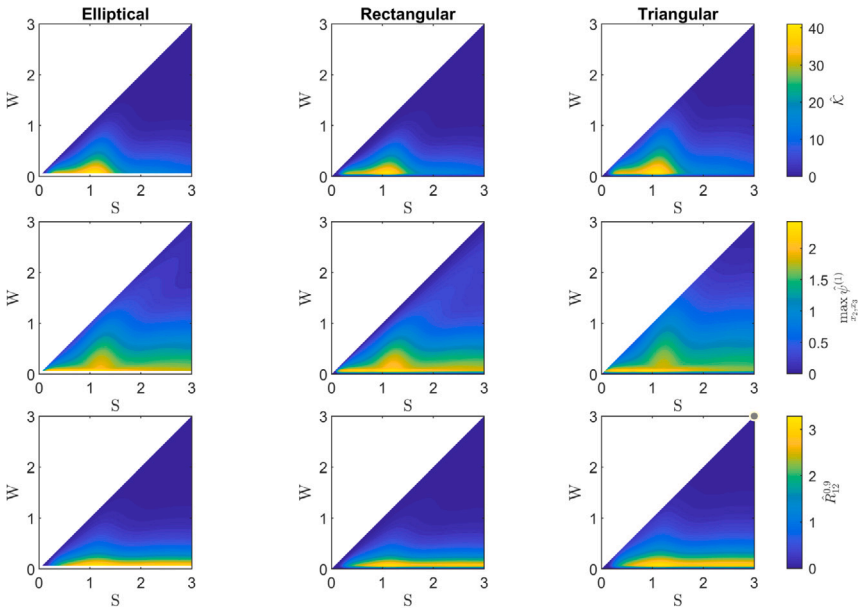

Fig. 3. Maps of the scaled kinetic energy density $\hat{\mathcal{K}}$ (top panels), the scaled maximum of the streamfunction $\max_{x_2,x_3} \hat{\psi}^{(1)}$ (central panels) and dispersive stress scaled $\hat{R}_{12}^{0.9}$ (bottom panels) are reported as a function of the ridge spacing S and ridge width W for $Re_\tau = 1000$ for elliptical ridges (left column), rectangular ridges (central column) and triangular ridges (right column).

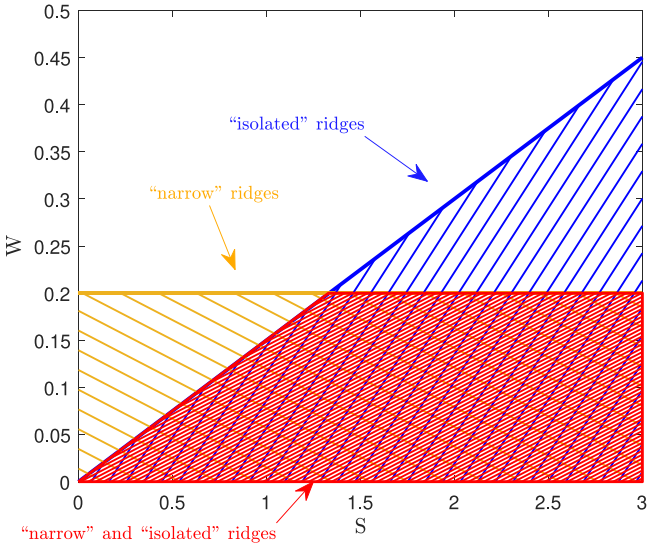

Fig. 4. Diagram showing qualitatively the regions in parameter space defining "narrow" ridges (yellow area), "isolated" ridges (blue area), and the scaling region where the ridges are both "narrow" and "isolated" (red area). The boundaries of these regions are arbitrary, here we take $W < 0.2$ for narrow ridges and $W/S < 0.15$ for isolated ridges. (For interpretation of the references to colour in this figure legend, the reader is referred to the web version of this article.)

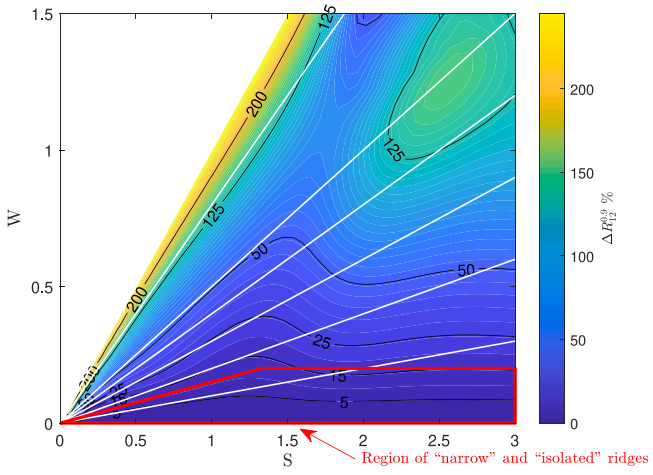

Fig. 5. Map of the quantity is $\Delta\hat{R}_{12}^{0.9}\%$. The black contours are plotted for $\Delta\hat{R}_{12}^{0.9}\% = 5, 15, 25, 50, 125$ and 200%. The white straight lines are obtained for a constant duty cycle $DC = 0.1, 0.2, 0.3, 0.4, 0.5$ and 0.8, moving from the bottom to the upper line. The region defining "narrow" and "isolated" ridges is also reported in the figure.

profiles differ and no collapsing is observed. Close to the wall (panel a), the velocity profiles show a peak value that depend on the ridge geometry. This is due to the proximity to the ridge that locally modify the flow field. For increasing width (panel b and c), the velocity profiles differ. The ridge geometry affects the peak value (higher for triangular ridges). For increasing W, the strength of the vortices decreases, too. Similarly, the wall-normal velocity at the centre of the trough is plotted in panels (d,e,f) of Fig. 6. These velocity profiles collapse for the entire channel height only for the isolated ridge configuration ($W = 0.2$). To explain the collapse of the profiles at the centre of the trough for narrow *and* isolated ridges, one can observe that the secondary flows at the centre of the trough are not affected by the ridge geometry, since the distance from the nearest ridge is large compared with W. The peak value slightly changes for $W = 0.67$. For $W = 1.0$ where the gap is reduced, the velocity profiles are strongly dependent on the ridge geometry and its effect is not negligible when moving towards the centre of the channel. However, a collapse of the curves is still observed in the near wall region where the influence of the ridges is weak. For all three geometries and for $W = 0.2$, the spanwise velocity profiles in the bottom panels collapse along the entire wall-normal direction. A negative peak is predicted at the wall over the ridge edge where the Reynolds stresses are stronger. Except for the case $W = 0.2$, the peak value depends on the ridge geometry. Moving towards the channel centre, the velocity decreases in magnitude. For increasing width, the scaling breaks down and some differences can be observed across the three geometries.

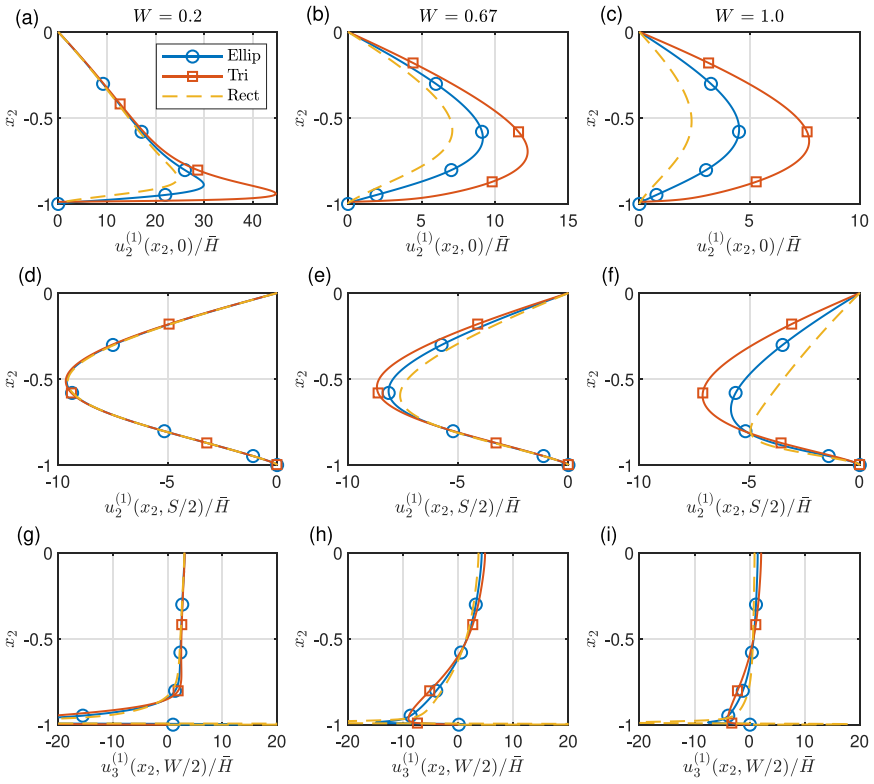

Fig. 6. Scaled profiles of the wall-normal velocity component at the centre of the ridge (top panels) and at the centre of the gap (central panels). The spanwise velocity component is obtained at the ridge edge (bottom panels). The spacing is $S = 1.25$ and the ridge width $W = 0.2$ (left column), 0.67 (central column) and 1.0 (right column). The profiles are obtained for the elliptical "Ellip", triangular "Tri" and rectangular "Rect" ridges for $Re_\tau = 1000$.

6. Tertiary flows over trapezoidal ridges

In the previous sections, we investigated simple geometries and the flow structure and strength as a function of the geometrical parameters S and W. We observed that secondary flows develop on the ridge edge where there is a strong discontinuity in the ridge shape. This is particularly true for both elliptical and rectangular ridges while for triangular ridges, secondary flows always develop at the ridge crest. Tertiary flows were only observed for the triangular ridges at the given configuration $DC = 0.5$ and $W = 1$ as shown in Fig. 1. This configuration is characterized by wide and sparse ridges and lies outside the parameter space where the scaling of the strength of the secondary flows has been properly observed. We can define this region of the parameter space as the scaling region and it involves the configurations characterized by narrow *and* isolated ridges. Thus, we can conclude that the scaling behaviour does not hold when tertiary flows appear. Trapezoidal ridges are here studied because they combine the main properties of both rectangular and triangular ridges. This allows to better understand how the combination of the shape properties affects the generation of the secondary and tertiary flows. It is worth noting that for the ridge shapes showing a strong discontinuity, the secondary flows are locked at a ridge edge.

For this purpose, in addition to the spacing S and the ridge width W, we introduce a third geometrical parameter α as the ratio between the minor and major bases of the ridges. A sketch of the ridges considered is shown in Fig. 7 on the left-hand side of the corresponding flow topology. Note that triangular and rectangular ridges are the two limit cases corresponding to $\alpha = 0$ and $\alpha = 1$, respectively. The flow organization as a function of α is reported in Fig. 7 for $S = 1.25$ and $W = 0.65$ at $Re_\tau = 1000$ (see the sketches on the left). Starting from triangular ridges, tertiary flows develop at the centre of the troughs while the secondary flows develop over the flank of the ridge. When α increases, the secondary currents slightly moves towards the ridge edges and the tertiary flows decrease in size and strength, until they disappear at $\alpha = 0.95$. In particular, tertiary flows emerge when the space between the secondary flows is large enough. This also explains why for a fixed configuration, characterized by large spacing and width, different shapes show different flow topologies.

The strength of secondary flows is then obtained for the trapezoidal ridges at varying α. The kinetic energy density $\mathcal{K}$ is reported in Fig. 8 where the contours of $\mathcal{K}$ for $\alpha = 0.25, 0.5$ and 0.8 are superimposed to the colour map of $\mathcal{K}$ for the rectangular ridges (see the caption for the figure for more details). The peak amplification changes slightly with α. For $\alpha = 0.25$, the peak amplification occurs for a slightly higher W than the rectangular ridges (black lines). In addition, the second amplification peak observed for a constant width changes slightly. It is worth noting that for trapezoidal ridges we predict a secondary peak for large width that is not observed for triangular ridges.

7. Conclusions

The model proposed in Zampino et al. (2022) is utilized in this paper to predict the structure of secondary flows produced by elliptical, triangular, rectangular and trapezoidal ridges. The time-averaged flow field over such surfaces is decomposed into a base flow developing in the flat channel, and a flow perturbation induced by the ridges. In the limit of shallow ridges, linearized equations are obtained for the perturbation streamwise velocity and the perturbation streamfunction. These equations are complemented by inhomogeneous boundary conditions at the wall that capture the effect of the ridge. Since the equations are linear, the superposition principle is applied to reconstruct the flow field over complex geometries. The model is computationally cheap and allows a rapid evaluation of a variety of ridge configurations.

Results for $Re_\tau = 1000$ are reported. Strong similarities in the configuration of the secondary flows are observed for narrow ridges with small width compared to the spacing. Starting from the narrow ridge

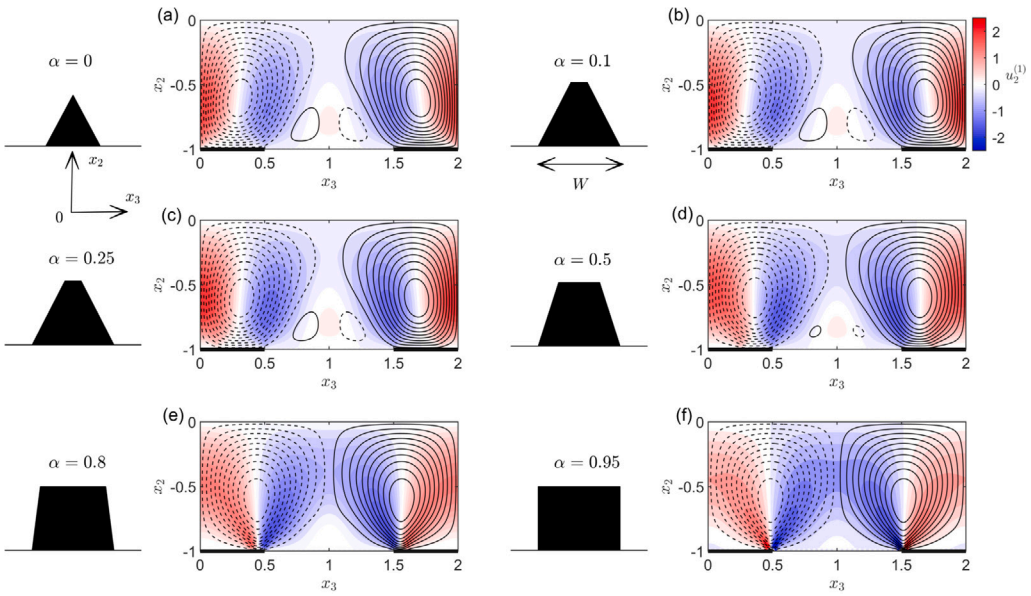

Fig. 7. Secondary flows generated by trapezoidal ridges at $Re_\tau = 1000$ and for $(S, W) = (2, 1)$. The shape parameter α varies from 0, corresponding to a triangular ridge in panel (a), to 0.95, corresponding to a rectangular ridge in panel (f). The value of α is reported. For the sake of clarity, a sketch of the ridge shape is also provided for each configuration studied.

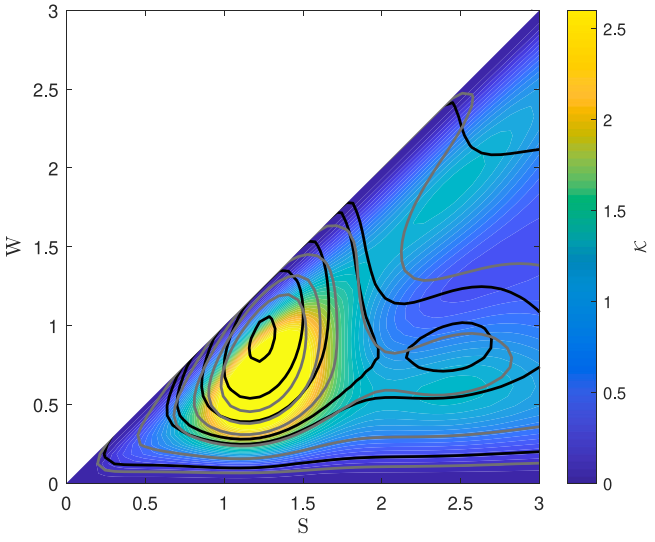

Fig. 8. Maps of the kinetic energy density $\mathcal{K}$ of the secondary flows over trapezoidal ridges as a function of the spacing S and width W. The colour map corresponds to the strength of the secondary flows generated by the rectangular ridges. The dark grey lines corresponds to the contour of the triangular ridges while the light grey lines are obtained for the trapezoidal ridges with $\alpha = 0.5$. The contour levels are $\mathcal{K} = [0.5, 0.6, 1, 1.1, 1.5, 2, 2.5]$. The Reynolds number is $Re_\tau = 1000$.

configuration, for a fixed spacing and increasing width, the vortices grow in strength and size until they occupy the channel half-height. The flow organization differs between the three geometries for wide ridges where the secondary structures depend on the ridge geometry.

The similarity in the flow topology for narrow ridges suggest that the velocity induced can be scaled using an appropriate parameter that depends on the ridge geometry. Since the ridges are localized at the wall, the effect of the wall perturbation is assumed to be proportional to the cross-sectional area of the ridges, not their geometry. For this reason, the mean ridge height $\overline{H} = A_r/S$ is here proposed as the scaling parameter.

In particular, the maps of the volume averaged dispersive stresses scaled with $\overline{H}^2$ collapse for ridge configurations with small width W, defining the "narrow ridge" regime, *and* high ratio S/W, defining the "isolated ridges" regime. For these configurations the effect of the ridge geometry is negligible or confined to the very near-wall region and the scaled velocity profiles collapse. In particular, the collapse of the profiles at the centre of the trough can be explained as the consequence of the low influence of the nearest ridge. For increasing width, the scaling behaviour breaks down because the flow topology strongly depends on the ridge geometry. Finally, the generation mechanism of the tertiary flows is studied for trapezoidal ridges. The present paper confirms that tertiary flows emerge when the space between the secondary flows is large enough. These results extend the conclusions about the generation of tertiary flows for rectangular ridges by Zampino et al. (2022) to more general shapes.

Some remarks on the limitations of the model are in order. One of the key modelling assumptions is that the ridge height is infinitesimal, i.e. the topography variation is shallower than any other dynamically-relevant length scale in the flow, e.g. the viscous length scale. Physically, this regime corresponds to topographies that are fully submerged in the viscous sub-layer. Such a topography creates a lateral variation of the origin from which the turbulent wall-bounded flow develops, and results in spanwise gradients of the Reynolds stresses throughout the turbulent layer. In turn, these feed into the momentum equations as source terms, resulting in the generation of secondary currents (Perkins, 1970). For shallow topographies, the flow response is expected to be linear, in the sense that the perturbation velocities, e.g. the cross-stream components, are linearly proportional to the amplitude of the topography (Luchini, 2013; Russo and Luchini, 2016). However, the vast majority of studies on secondary currents have considered rather tall ridges that protrude well into the log layer, with a height that is a non-negligible fraction of the shear flow thickness. Secondary currents developing over surfaces with prominent ridges are likely not captured satisfactorily by the present model, because the shallow-topography assumption does not apply for such geometries. This is especially true for ridges characterized by highly sloped flanks, e.g. rectangular ridges. In such cases, a strong interaction between the instantaneous turbulent fluctuations and the ridge is to be expected, such as the upwards deflection of the spanwise velocity fluctuations discussed in Hwang and Lee (2018). In summary, as the ridge height is increased, it is likely that the flow-ridge interaction transitions through a range of different flow regimes. Detailed exploration of these regimes has started only

recently (see e.g. von Deyn et al. (2022)). Effort should be dedicated in the future to clarify such transitions and capture relevant mechanism with simple models, to extend the present results to real-world surfaces with finite-height ridges.

CRediT authorship contribution statement

Gerardo Zampino: Conceptualization, Methodology, Software, Validation, Formal analysis, Investigation, Data curation, Writing – original draft, Visualization. **Davide Lasagna:** Conceptualization, Study design, Formal analysis, Resources, Writing – review & editing, Project administration. **Bharathram Ganapathisubramani:** Conceptualization, Supervision, Editing, Project administration, Funding acquisition.

Declaration of competing interest

The authors declare that they have no known competing financial interests or personal relationships that could have appeared to influence the work reported in this paper.

Data availability

Data will be made available on request.

Acknowledgment

The authors acknowledge the Engineering and Physical Sciences Research Council for the financial support (EP/V00199X/1).

References

Anderson, W., Barros, J.M., Christensen, K.T., Awasthi, A., 2015. Numerical and experimental study of mechanisms reponsible for turbulent secondary flows in boundary layer flows over spanwise heterogeneous roughness. J. Fluid Mech. 768, 316–347.

Barros, J.M., Christensen, K.T., 2014. Observation of turbulent secondary flows in a rough-wall boundary layer. J. Fluid Mech. 748, R1.

Bottaro, A., Soueid, H., Galletti, B., 2006. Formation of secondary vortices in turbulent square-duct flow. AIAA J. 44, 803–811.

Busse, A., Sandham, N.D., 2012. Influence of an anisotropic slip-length boundary condition on turbulent channel flow. Phys. Fluid 24, 055111.

Castro, I.P., Kim, J.W., Stroh, A., Lim, H.C., 2021. Channel flow with large longitudinal ribs. J. Fluid. Mech. 915, A92.

Cess, R.D., 1958. A survey of the literature on heat transfer in turbulent tube flow. Technical Report 8-0529-R24, Westinghouse Research.

Chen, W.L., Lien, F.S., Leschziner, M.A., 1997. Non-linear eddy-viscosity modelling of transitional boundary layers pertinent to turbomachine aerodynamics. Int. J. Heat Fluid Flow 19, 297–306.

Chung, D., Monty, J.P., Hutchins, N., 2018. Similarity and structure of wall turbulence with lateral wall shear stress variations. J. Fluid Mech. 847, 591–613.

del Álamo, J.C., Jiménez, J., 2006. Linear energy amplification in turbulent channels. J. Fluid Mech. 559, 205–213.

Hinze, J.O., 1967. Secondary currents in wall turbulence. Phys. Fluids 10 (9), 122–125.

Hwang, H.G., Lee, J.H., 2018. Secondary flows in turbulent boundary layers over longitudinal surface roughness. Phys. Rev. Fluids 3, 014608.

Jiménez, J., 2004. Turbulent flows over rough walls. Annu. Rev. Fluid Mech. 36, 173–196.

Knoll, D.A., Keyes, D.E., 2004. Jacobian-free Newton-Krylov methods: a survey of approaches and applications. J. Comput. Phys. 193, 357–397.

Luchini, P., 2013. Linearized no-slip boundary conditions at rough surface. J. Fluid Mech. 737, 349–367.

Medjnoun, T., Vanderwel, C., Ganapathisubramani, B., 2018. Characteristics of turbulent boundary layers over smooth surfaces with spanwise heterogeneities. J. Fluid Mech. 838.

Medjnoun, T., Vanderwel, C., Ganapathisubramani, B., 2020. Effects of heterogeneous surface geometry on secondary flows in turbulent boundary layers. J. Fluid Mech. 886, A31.

Mejia-Alvarez, R., Christensen, K., 2013. Wall-parallel stereo particle-image velocimetry measurements in the roughness sublayer of turbulent flow overlying highly irregular roughness. Phys. Fluids 25, 015106.

Perkins, H.J., 1970. The formation of streamwise vorticity in turbulent flow. J. Fluid Mech. 44, 721–740.

Prandtl, L., 1952. Essentials of Fluid Dynamics. Hafner.

Pujals, G., Garcìa-Villalba, M., Cossu, C., Depardon, S., 2009. A note on optimal transient growth in turbulent channel flows. Phys. Fluids 21, 015109.

Reynolds, W.C., Hussain, A.K.M.F., 1972. The mechanism of an organized wave in turbulent shear flow. Part 3. theoretical models and comparisons with experiments. J. Fluid Mech. 54, 263–288.

Russo, S., Luchini, P., 2016. The linear response of turbulent flow to a volume force: comparison between eddy-viscosity model and DNS. J. Fluid Mech. 790, 104–127.

Spalart, P.R., 2000. Strategies for turbulence modelling and simulations. Int. J. Heat Fluid Flow 21, 252–263.

Spalart, P.R., Allmaras, S.R., 1994. A one-equation turbulence model for aerodynamic flows. Rech. Aerosp. 1, 5–21.

Spalart, P.R., Garbaruk, A., Stabnikov, A., 2018. On the skin friction due to turbulence in ducts of various shapes. J. Fluid Mech. 838, 369–378.

Speziale, C.G., 1991. Analytical methods for the development of Reynolds-stress closures in turbulence. Annu. Rev. Fluid Mech. 23, 107–157.

Speziale, C.G., Sarkar, S., Gatski, T.B., 1991. Modelling the pressure-strain correlation of turbulence: an invariant dynamical system approach. J. Fluid Mech. 227, 254–272.

Stroh, A., Schäfer, K., Forooghi, P., Frohnapfel, B., 2020. Secondary flow and heat transfert in turbulent flow over streamwise ridges. Int. J. Heat Fluid Flow 81, 108518.

Stroh, A., Y. Hasegawa, J.K., Frohnapfel, B., 2016. Secondary vortices over surfaces with spanwise varying drag. J. Turbul. 17, 1142–1158.

Vanderwel, C., Ganapathisubramani, B., 2015. Effects of spanwise spacing on large-scale secondary flows in rough-wall turbulent boundary layers. J. Fluid Mech. 774, R2.

Volino, R.J., Schultz, M.P., Flack, K.A., 2011. Turbulence structure in boundary layers over periodic two- and three-dimensional roughness. J. Fluid Mech. 676, 172–190.

von Deyn, L.H., Gatti, D., Frohnapfel, B., 2022. From drag-reducing riblets to drag-increasing ridges. J. Fluid Mech. 951, A16. http://dx.doi.org/10.1017/jfm.2022.796.

Willingham, D., Anderson, W., Christensen, K.T., Barros, J.M., 2014. Turbulent boundary layer flow over transverse aerodynamic roughness transitions: induced mixing and flow characterization. Phys. Fluids 26, 025111.

Wu, Y., Christensen, K.T., 2007. Outer-layer similarity in the presence of a practical rough-wall topography. Phys. Fluids 19, 085108.

Zampino, G., Lasagna, D., Ganapathisubramani, B., 2022. Linearised Reynolds-averaged predictions of secondary currents in turbulent channels with topographic heterogeneity. J. Fluid Mec. 944, A4.

Zampiron, A., Cameron, S., Nikora, V., 2020. Secondary currents and very-large-scale motions in open-channel flow over streamwise ridges. J. Fluid Mech. 887, A17.